Icarus 273 (2016) 182–195

Contents lists available at ScienceDirect

Icarus

journal homepage: www.elsevier.com/locate/icarus

Lunar crater ejecta: Physical properties revealed by radar and thermal infrared observations

R.R. Ghent[a,b,*], L.M. Carter[c], J.L. Bandfield[d], C.J. Tai Udovicic[a], B.A. Campbell[e]

[a] Dept of Earth Sciences, University of Toronto, Toronto, ON M5S 3B1, Canada
[b] Planetary Science Institute, Tucson, AZ 85719, United States
[c] NASA Goddard Space Flight Center, Greenbelt, MD 20771, United States
[d] Space Science Institute, Boulder, CO 80301, United States
[e] Center for Earth and Planetary Studies, Smithsonian Institution, Washington, DC 20013, United States

ARTICLE INFO

Article history:
Received 30 June 2015
Revised 8 November 2015
Accepted 9 December 2015
Available online 24 December 2015

Keywords:
Moon
Regoliths
Radar observations
Infrared observations
Cratering

ABSTRACT

We investigate the physical properties, and changes through time, of lunar impact ejecta using radar and thermal infrared data. We use data from two instruments on the Lunar Reconnaissance Orbiter (LRO) – the Diviner thermal radiometer and the Miniature Radio Frequency (Mini-RF) radar instrument – together with Earth-based radar observations. We use this multiwavelength intercomparison to constrain block sizes and to distinguish surface from buried rocks in proximal ejecta deposits. We find that radar-detectable rocks buried within the upper meter of regolith can remain undisturbed by surface processes such as micrometeorite bombardment for >3 Gyr. We also investigate the thermophysical properties of radar-dark haloes, comprised of fine-grained, rock-poor ejecta distal to the blocky proximal ejecta. Using Diviner data, we confirm that the halo material is depleted in surface rocks, but show that it is otherwise thermophysically indistinct from background regolith. We also find that radar-dark haloes, like the blocky ejecta, remain visible in radar observations for craters with ages >3 Ga, indicating that regolith overturn processes cannot replenish their block populations on that timescale.

1. Introduction

Impact cratering and volcanism represent the two fundamental geological processes that have operated on the Moon for the past 4.6 Gyr. Cratering has created the large-scale architecture of the Moon's surface, it creates and overturns lunar regolith, and it profoundly affects the physical characteristics of lunar surface materials at all spatial scales. Many aspects of the history of the Moon are hidden in the history of impact cratering. An understanding of the time-dependent impact flux, and how we interpret that rate as it is expressed in the cratering record, forms the basis of lunar chronology (e.g., Neukum et al., 2001). A handful of lunar ejecta samples anchor the lunar crater-based chronology to the absolute timescale, and the only available method for dating terrains and features on other planets is to extrapolate from the lunar case. Therefore, a deep understanding of lunar cratering is vital to understanding cratering and chronology elsewhere in the Solar System.

Analysis of impact craters is a major component of the study of any planetary surface. Implicit in this analysis is an interpretation of the effects of physical processes responsible for creating the crater and modifying it. In particular, impact ejecta morphologies and physical properties have long been used to deduce characteristics of the target terrains (e.g., Quaide and Oberbeck, 1968; Baratoux et al., 2005; Wada and Barnouin-Jha, 2005; Barlow, 2006; van der Bogert et al., 2010, 2013; Williams et al., 2014). The Moon provides a limiting case for understanding these processes because it is an airless body with no atmospheric influence on ejecta distribution and no aeolian or weather-induced alteration of craters. In this paper, we explore the physical properties of lunar ejecta and seek to link them to underlying impact processes and target properties.

The purpose of this work is: (a) to characterize and, where possible, to quantify, the physical properties of lunar impact ejecta, using both radar and thermal IR data; and (b) to investigate the evolution in these characteristics with time. It is well understood that lunar impacts excavate material from within and beneath the regolith and distribute the resulting ejecta on the surface. With new datasets provided by the Lunar Reconnaissance Orbiter (LRO), together with Earth-based radar, we now have the opportunity to

* Corresponding author at: Dept of Earth Sciences, University of Toronto, 22 Russell St., Toronto, ON M5S 3B1, Canada.

http://dx.doi.org/10.1016/j.icarus.2015.12.014
0019-1035/

gain new information about the physical properties of surface and buried impact ejecta that is not otherwise available.

The LRO spacecraft has produced global or near-global radar, infrared and optical remote sensing data. In particular, the Mini-RF instrument obtained 66% coverage of the lunar surface, including imaging of the farside, which is not possible from Earth (e.g. Cahill et al., 2014). In addition, the spectral resolution of the new LRO thermal IR data has allowed quantitative estimates of rock abundance and regolith temperature (Bandfield et al., 2011) and regolith thermal inertia (Hayne et al., 2011). The spatial resolution of these new datasets represents more than a factor of two increase over those used in the previous radar–thermal infrared comparison studies outlined in the next section. These improvements afford the opportunity to gain a much deeper understanding of ejecta properties, and their emplacement mechanisms, than ever before.

2. Previous work

An extensive body of literature on the radar and thermal infrared properties of ejecta has been created over the past 50 years. Blocky ejecta produce high radar backscatter (e.g., Thompson et al., 1974, 1979, 1981) and high circular polarization ratios (e.g., Campbell, 2012) due to scattering of incident energy from multiply-oriented facets and internal reflections. These effects are wavelength-dependent, and comparisons of radar signatures at different wavelengths have produced constraints on the block sizes present in ejecta at various distances from the parent crater. Comparisons of radar and thermal infrared observations provide further insight; nighttime temperatures of rocks and regolith materials are controlled by thermal inertia, which determines heating and cooling rates during the lunar night and during eclipses. These two different timescales provide information about material properties at different characteristic depths (e.g., Hayne et al., 2011). Previous work comparing 10 μm thermal infrared nighttime and eclipse data and 3.8- and 70-cm wavelength radar images of lunar craters (Shorthill et al., 1972; Thompson et al., 1974, 1979; Schultz and Mendell, 1978) revealed a range of responses. For instance, Thompson et al. (1974) found that in some cases, elevated eclipse temperatures were correlated with elevated radar backscatter at both wavelengths. This suggested the presence of surface rocks at a variety of sizes to generate both high radar backscatter at short and long wavelengths, and high eclipse temperatures. Other terrains lacked such strong enhancement at IR wavelengths but were bright in one or both radar data sets. This implied that the radar data detected a population of buried rocks that were not visible to the infrared data. In other areas, high infrared temperatures correlated with low radar backscatter at one or both wavelengths suggested a population of surface rocks with certain sizes. Previous studies such as this one were generally qualitative in nature and used data with resolutions of hundreds of meters to 5 km per pixel; nevertheless, they provided key information about the how regolith rock sizes and structure vary across the Moon. We continue this line of investigation using the new data provided by LRO and Earth-based radar observations.

We have previously reported on the radar characteristics of haloes with low radar return found distal to the rocky continuous ejecta. These haloes, not visible in optical wavelength images (and distinct from dark mantle deposits and other features commonly associated with pyroclastic materials or crytomaria; see Hawke and Bell, 1982; Wilhelms, 1987), were first recognized in Earth-based radar images by Thompson et al. (1970, 1974). Schultz and Mendell (1978) noted anomalously low nighttime temperatures associated with some of these radar-detected features, and suggested that they represent impact-comminuted material depleted in large blocks. Ghent et al. (2005) analyzed these radar-dark haloes using new radar data, and, in agreement with Schultz and Mendell, also proposed that they are comprised of a thick deposit of fine-grained ejecta depleted in rocks. Ghent et al. (2008, 2010) further documented the nature of the haloes' margins and their sizes relative to their parent craters. Here, we examine these features further, and discuss their thermophysical signatures and implications for their emplacement.

3. Data

Multi-wavelength radar is an excellent remote sensing tool for regolith studies because the depth of penetration of the radar wave depends on the wavelength and on the properties of the material. Generally, for average material dielectric parameters, radar waves are capable of penetrating about ten times the wavelength into the surface. In addition, surface and buried objects (e.g., blocky ejecta fragments) scatter and reflect radar signals with wavelengths up to approximately ten times their size; so 10 cm rocks could scatter radar signals with up to 1 m wavelength. These wavelength-dependent phenomena afford the opportunity to probe to different depths, and to detect scatterers of different sizes, in different locations (Fig. 1), using the range of radar data now available.

Thermal infrared (8–100 μm) data are sensitive to the thermophysical properties of a much shallower fraction of the regolith. The sensing depth of thermal IR temperature measurements depends on the material and the timing of the diurnal cycle; for lunar regolith fines it is ~5–10 cm and for solid rock it is ~0.5–1 m (Nowicki and Christensen, 2007; Bandfield et al., 2011). Thus, thermal IR data allow us to quantify the physical properties of the shallow regolith, complementing observations made using radar, and the comparison of the two datasets can reveal variations in regolith properties with depth (up to the sensing depth of the longest-wavelength radar being used).

3.1. Radar datasets

In this paper, we use radar observations from the LRO Miniature Radio Frequency (Mini-RF) instrument, and Earth-based radar images acquired in bistatic geometry using the Arecibo Observatory (hereafter, AO) and Green Bank Telescope (hereafter, GBT) at P-band (f = 430 MHz, or 70 cm wavelength) and S-band (f = 2380 MHz, or 12.6 cm wavelength). The Mini-RF instrument operated at S-band and C-band wavelengths; here, we use S-band data. Most of the Mini-RF data were collected as S-band (12.6 cm wavelength) in a "zoom" mode with a pixel resolution of 15 × 30 m. Unlike Arecibo, Mini-RF used a hybrid polarity technique, transmitting circular polarization and receiving the H (horizontal) and V (vertical) linear polarizations (Raney et al., 2011). Mini-RF transmit signals were inherently elliptically polarized (Raney et al., 2011), but because the entire Stokes matrix was collected, the circular polarization ratio can be calculated from the individual Stokes components. Here, we use Mini-RF total power and CPR images at the highest resolution 15 m/pixel (Cahill et al., 2014).

The Earth-based radar signals are circularly polarized, and the circular polarization ratio, or CPR, is highly sensitive to the presence of volumetric scattering (e.g., Campbell, 2012). In this paper, we refer to these products for the two available wavelengths as AO-GBT P-band or AO-GBT S-band CPR. P-band data are processed to a sampling of 400 m/pixel, and S-band images are 80 m/pixel. Earth-based radar observations are described in detail in Campbell et al. (2007).

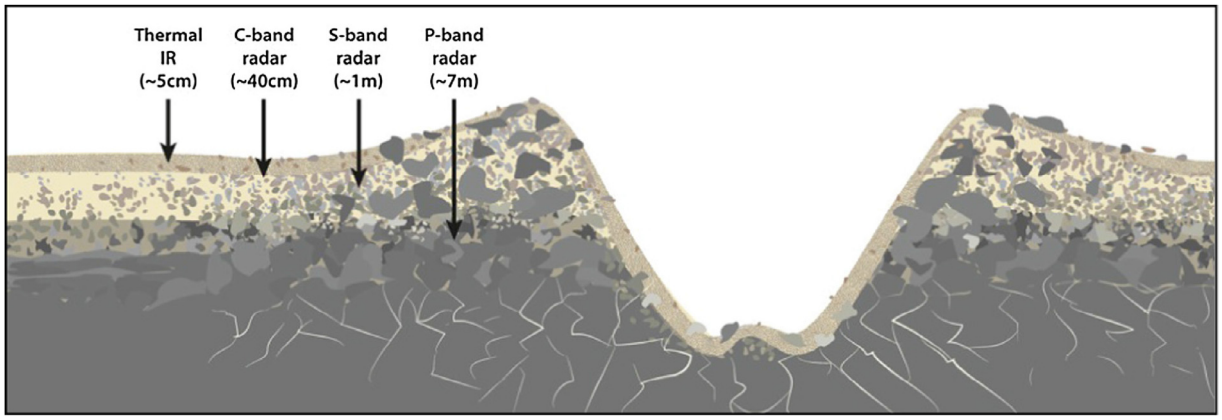

Fig. 1. Notional cross-section through an impact crater and its ejecta, showing characteristic depth sensitivities of thermal IR and radar datasets (image: NASA/GSFC/J. Friedlander).

3.2. Diviner Radiometer data

Diviner is a nine-channel radiometer with seven thermal infrared (TIR) channels covering ~8–300 μm in wavelength (Paige et al., 2009). We primarily use the gridded Diviner rock abundance (RA) and regolith temperature products derived from channels 6–8 (13–100 μm wavelengths; Bandfield et al., 2011). These two quantities are calculated by exploiting the fact that dense, high thermal inertia rocks sustain higher temperatures during the lunar night than do fine regolith materials, which have lower thermal inertia. Terrain that contains a mixture of large rocks and fine regolith produces different brightness temperatures from the measured radiance in each channel. This "anisothermality" can be used, together with modeled rock temperatures, in a least-squares minimization retrieval process to calculate two parameters: the abundance of rocks; and the temperature of the remaining fine regolith material. Rock abundance values are reported as the fraction of each field of view occupied by exposed rocks (or material with rock-like thermal inertia, and large enough to stay warm through the lunar night). A rock abundance value of 0.01 means that 1% of the relevant pixel is occupied by exposed rock, or rocks, of size greater than the diurnal thermal skin depth (roughly 1 m), and with little or no regolith cover. Regolith temperature is reported in degrees Kelvin relative to the longitudinal average at the corresponding latitude, and is normalized both for latitude and local time. These two datasets have been produced for all longitudes and latitudes from 80 S to 80 N using 46 orbital cycles, and gridded to a sampling of 128 pixels per degree (236 m/pixel at the equator), and are available at http://pds-geosciences.wustl.edu/missions/lro/diviner.htm.

4. Ejecta properties

In this paper, we illustrate the physical properties of ejecta using the craters listed in Table 1. We chose these craters because they have a range of sizes and ages that allow us to track the properties of crater ejecta as they weather through time.

4.1. A note on crater ages

Determination of absolute ages of individual craters is a challenging endeavor. On planetary surfaces, dating is generally accomplished by using the size–frequency statistics of small craters superimposed on the terrain of interest, and relating them to a crater production function (see, for example, Hiesinger et al., 2012). That production function is anchored to the absolute timescale via a handful of radiometric and exposure ages measured for lunar samples (e.g., Stöffler and Ryder, 2001). For large impact craters, dates are usually determined by counting small craters superimposed on either the ejecta (e.g., Baldwin, 1985) or on the crater floors (e.g., Kirchoff et al., 2013). In either case, this effort requires differentiation of small primary from small secondary craters, robust identification of the underlying geological unit to be dated (either ejecta or crater floor materials), and choice of an appropriate production function. Complicating matters is the fact that counts made on crater floors or impact melt ponds consistently give younger ages than those derived from counts on ejecta blankets, due at least in part to variations in crater sizes arising from differences in the strength of the respective target materials (e.g., van der Bogert et al., this issue).

In Section 5, we examine how radar and thermal properties of crater ejecta change with time by studying craters of various ages. For consistency, we use the ages reported in Baldwin (1985) where direct comparisons between craters of different ages are required (e.g., Fig. 12). Elsewhere, we use the ages reported in Table 1, which gives both model ages and the reference for these ages.

4.2. Blocky ejecta

Most lunar craters show the radar signatures—high backscattered power and high circular polarization ratios—associated with the presence of rocky ejecta in annuli of varying width proximal to the crater rims (Thompson et al., 1974, 1979, 1981; Campbell et al., 2007; Campbell, 2012; Fig. 2). These characteristics arise from blocky ejecta either on the surface or buried within the penetration depth of the radar (e.g., Fig. 3). CPR data in particular are strongly sensitive to volumetric scattering (Campbell, 2002, 2012). However, because the radar signal originates from a volume of material up to tens of meters deep, it is not possible to distinguish surface from subsurface volumetric scattering using radar observations alone. Furthermore, though a CPR value of $\geqslant$1.0 means that the "depolarized" energy in the received signal is at least equal in magnitude to the "polarized" energy (e.g., Campbell et al., 2007), an effect caused by volumetric scattering, we cannot simply invert radar CPR values to determine block content. CPR values exceeding 1.0 are common in rocky ejecta deposits, and are best explained by a dominantly dipole-like scattering mechanism, in which scattering from randomly oriented cracks and rock edges in a volume interacts to produce the observed signal (Campbell, 2012). These effects are most likely mixed with dihedral scattering effects and single-bounce reflections from randomly oriented facets at a range of horizontal scales and depths, all moderated by the dielectric

Table 1
Study craters.

Crater	Center longitude	Center latitude	Diameter (km)	Age (myr)	Age reference
Aristarchus	312.5	23.7	42.0	148 −16/+20	Baldwin (1985)
Aristillus	1.2	33.8	55.9	1826 −213/+237	Baldwin (1985)
Aristoteles	17.2	50.2	94.9	2700 ± 800	Kirchoff et al. (2013)
Atlas	44.4	46.7	93.9	n/a	
Autolycus	1.5	30.7	38.0	834 −221/+260	Baldwin (1985)
Bullialdus	337.7	−20.8	62.5	3230 −480/+243	
Bürg	28.2	45.0	40.2	n/a	
Byrgius A	296.2	−24.6	18.7	48 ± 14.1	Morota et al. (2009)
Copernicus	339.9	9.6	99.6	834 −61/+69	Baldwin (1985)
Delisle	325.3	30.0	26.5	3470	Baldwin (1985)
Diophantus	325.7	27.6	18.6	911 −252/+297	Baldwin (1985)
Eratosthenes	348.7	14.5	60.0	2971 −175/+183	Baldwin (1985)
Euler	330.8	23.3	26.8	605 −198/+214	Baldwin (1985)
Giordano Bruno	102.9	36.0	22.1	4 ± 1.4	Morota et al. (2009)
Hercules	39.1	46.8	74.0	n/a	
Kepler	322.0	8.1	30.6	1063 −175/+191	Baldwin (1985)
Plinius	23.6	15.3	42.2	2985 −298/+116	Baldwin (1985)
Pytheas	339.4	20.5	19.6	682 −153/+175	Baldwin (1985)
Reiner	305.0	6.9	29.8	1140 −337/+412	Baldwin (1985)
Reinhold	337.1	3.2	45.7	2819 −245 + 267	Baldwin (1985)
Thales	50.3	61.7	33.3	n/a	
Timocharis	346.9	26.7	34.9	529 −92/+99	Baldwin (1985)
Tycho	348.8	−43.3	87.0	138 −20/+24	Baldwin (1985)
Vlacq	38.7	−53.4	89.2	3900 ± 100	Kirchoff et al. (2013)

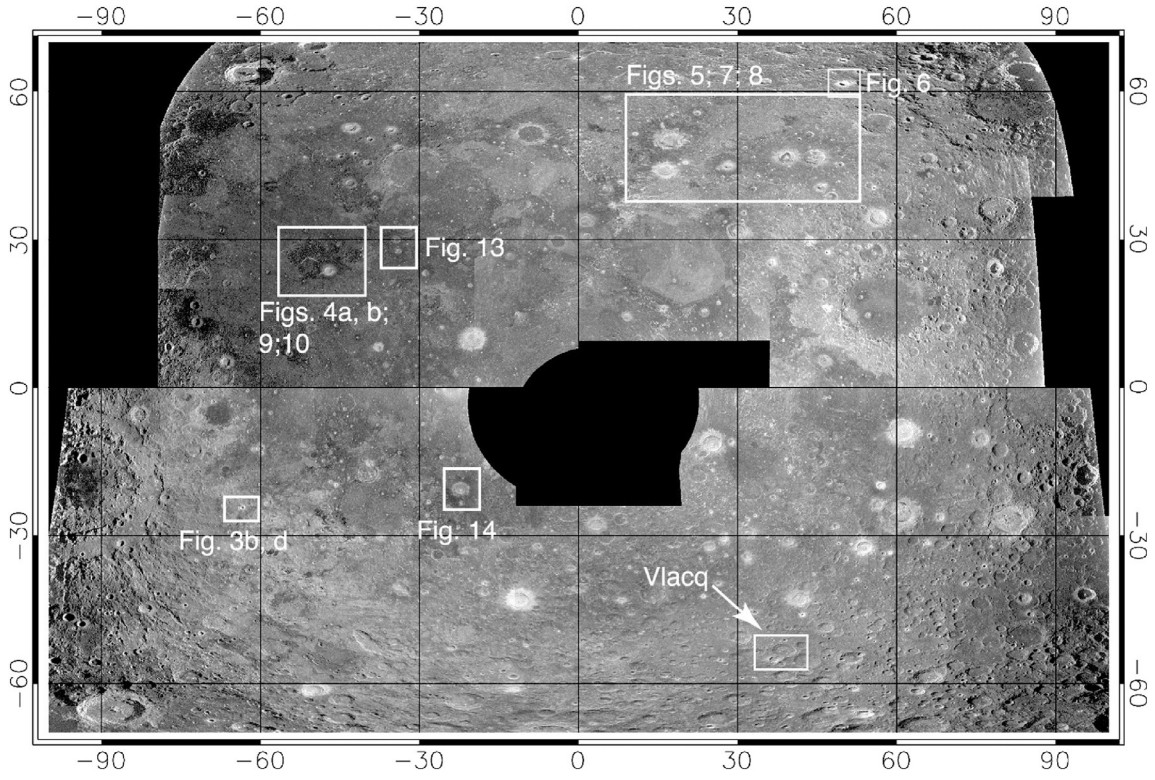

Fig. 2. AO-GBT P-band mosaic of the lunar nearside (Campbell et al., 2007); boxes show locations of subsequent figures and crater Vlacq (Section 5).

properties of each reflecting surface, which determine the fraction of incident energy reflected (Campbell, 2012). This extremely complicated physical scenario precludes simple association of specific CPR values with specific rock abundances. However, a CPR value of 1.0 in AO-GBT P-band observations can be understood to signal significant blockiness over the horizontal scale of a single pixel, or 400 m. The shorter wavelength AO-GBT S-band and Mini-RF data are sensitive to scatterers that are smaller by a factor of ~5, and their higher spatial sampling allows for resolution of smaller high CPR features. Therefore, discrepancies between the radar signals at these different wavelengths, and the spatial patterns they describe, are valuable tools in mapping out surface and subsurface ejecta.

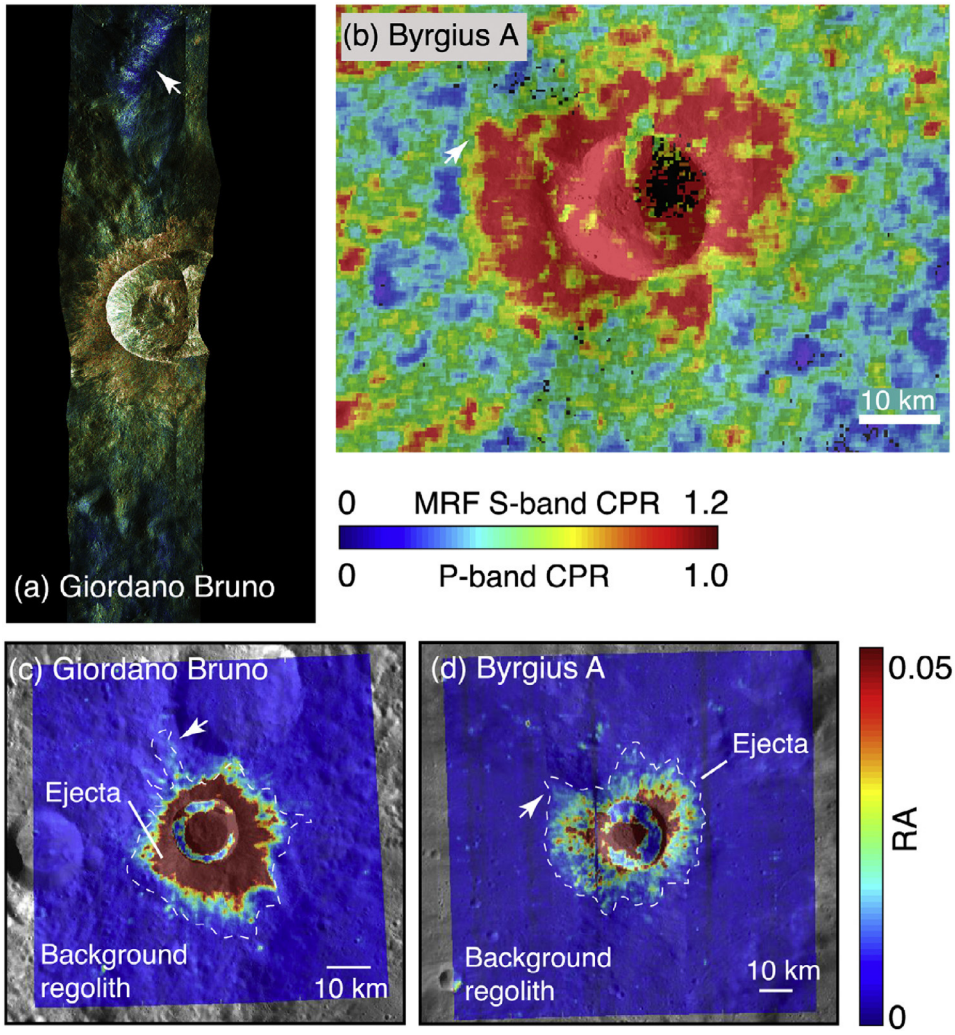

Fig. 3. Radar (a and b) and Diviner rock abundance (c and d) maps for two young rocky craters, Giordano Bruno and Byrgius A. (a) Mini RF CPR (color) overlain on total power at 15 m/pixel; (b) AO-GBT P-band CPR, 400 m/pixel. Arrows show corresponding features in the radar and Diviner images. (For interpretation of the references to color in this figure legend, the reader is referred to the web version of this article.)

Diviner rock abundance data, by contrast, are sensitive only to surface rocks. Young craters, such as Giordano Bruno and Byrgius A (Fig. 3; Table 1), both show elevated Diviner rock abundance values in their ejecta, characterized by distributions with long tails at high values (Ghent et al., 2014). We use the 95th percentile values to capture this distribution; they are >12% for Giordano Bruno (with a maximum value >40%), and 4.7% for Byrgius A. (Note that we exclude all terrain inward from the crater rims, where mass wasting on steep slopes replenishes the rock population.) Typical background regolith rock abundances, by contrast, are normally distributed about mean values ~0.5%. For these two young craters, the Diviner rock abundance signature is correlated with the radar signatures.

In other cases, Diviner rock abundance and radar signatures are not correlated. For instance, Fig. 4 shows AO-GBT CPR and Diviner RA maps for Aristarchus and Copernicus. In both cases, the radar maps show wispy, digitate ejecta near the outer edges of the radar-bright haloes that do not correspond to elevated rock abundance values. In fact, for Copernicus, the region corresponding to the radar-bright ejecta halo shows very little rock abundance enhancement. This discrepancy indicates that most of the blocks that give rise to the high radar CPR values reside in the subsurface, covered by a sufficient depth of insulating regolith to hide them from Diviner's view (see also Bandfield et al., 2011). One-dimensional thermal models (e.g., Hayne et al., 2011; Bandfield et al., 2014) suggest that these blocks are buried beneath a minimum of a few centimeters to tens of centimeters of regolith material.

Discrepancies between the magnitude or spatial distribution of CPR values can provide additional information about blocky ejecta. For example, Hercules crater (Fig. 5) shows two distinct regions of P-band radar enhancement associated with its proximal ejecta; higher CPR values with denser spatial distribution define an inner halo, and a sparser, digitate region of lower, but still elevated, CPR values defines an outer halo. The outer halo is not apparent in the S-band image (Fig. 5b), and the inner halo shows lower overall CPR values and a lower density of high CPR points than at P-band. In general, differences between CPR values at different wavelengths can be caused by variations in either block size or burial depth. In this case, in which scatterers that appear at P-band are invisible at S-band, block size is not likely to be the sole factor because rocks large enough to scatter the P-band signals would also scatter S-band signals, if they were within the S-band penetration depth. Therefore, we infer that all of the blocks responsible for the

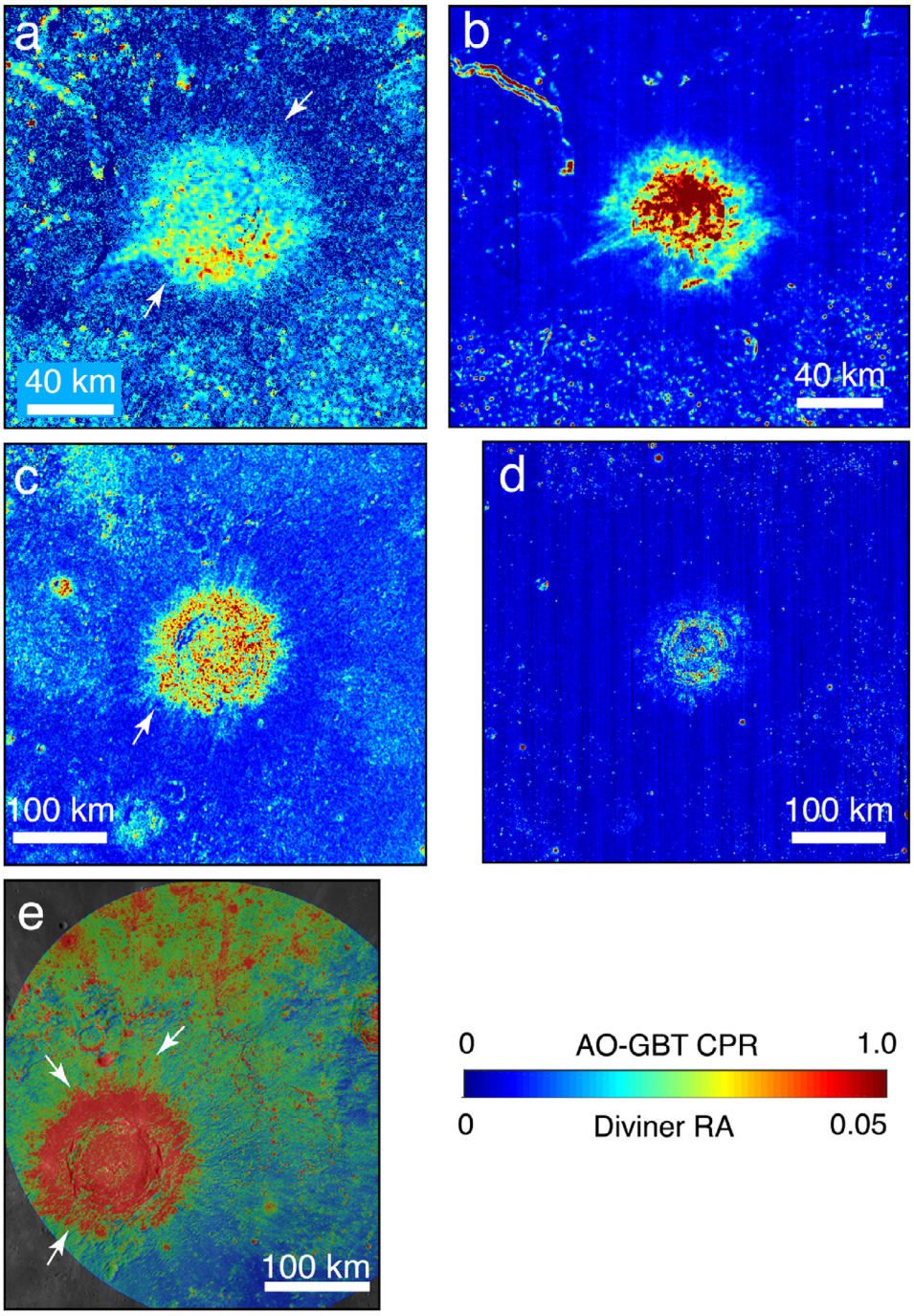

Fig. 4. (a and c) AO-GBT P-band CPR; (b and d) Diviner rock abundance; and (e) AO-GBT S-band CPR images of Aristarchus (a and b) and Copernicus (c–e). White arrows show regions of blocky ejecta indicated by elevated radar CPR, which do not appear in the corresponding rock abundance images.

outer P-band signature, and some of those that generate the inner P-band signature, are buried deeper than the S-band signals can sense ($>\sim$1 m).

For Atlas crater, the P-band CPR image shows a distinct asymmetry, with lobate or digitate regions of enhancement emanating from the crater toward the East. The pattern of ejecta reflected by the radar enhancement suggests an oblique impact from the West. Though the same pattern appears in the S-band image, the enhancement is not nearly as strong, and is much less uniform. As with Hercules, this indicates ejecta burial depths of 1 m or more for most of the blocks. The inner halo of Hercules crater shows some enhancement in Diviner rock abundance, with RA values slightly in excess of 1%, indicating the presence of surface rocks, but the halo of Atlas crater is essentially devoid of surface rocks, with RA values $<$0.8%.

In some cases, rock size is the dominant effect causing discrepancies between radar signals at different wavelengths. Crater Thales (Fig. 6) shows nearly the same distribution of enhancement in P- and S-band CPR images (from both Earth-based and Mini-RF observations) and Diviner rock abundance associated with near-rim rocky ejecta. However, a secondary region of S-band CPR enhancement extends far beyond the inner region, and shows wispy margins at distances of several crater diameters. The rocks responsible for this S-band enhancement do not cause an enhancement in the

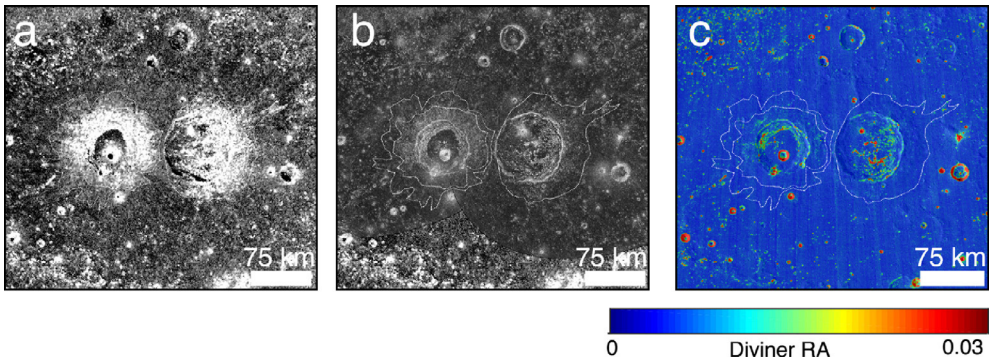

Fig. 5. Craters Hercules (left; 39.1 E, 46.8 N, $d = 74$ km) and Atlas (right; 44.4 E, 46.7 N, $d = 93.8$ km). (a) AO-GBT P-band CPR, at 400 m/pixel; (b) AO-GBT S-band CPR, at 80 m/pixel; (c) Diviner RA (0–3%). Dotted outlines denote boundaries of radar-bright ejecta, drawn using the P-band image shown in a.

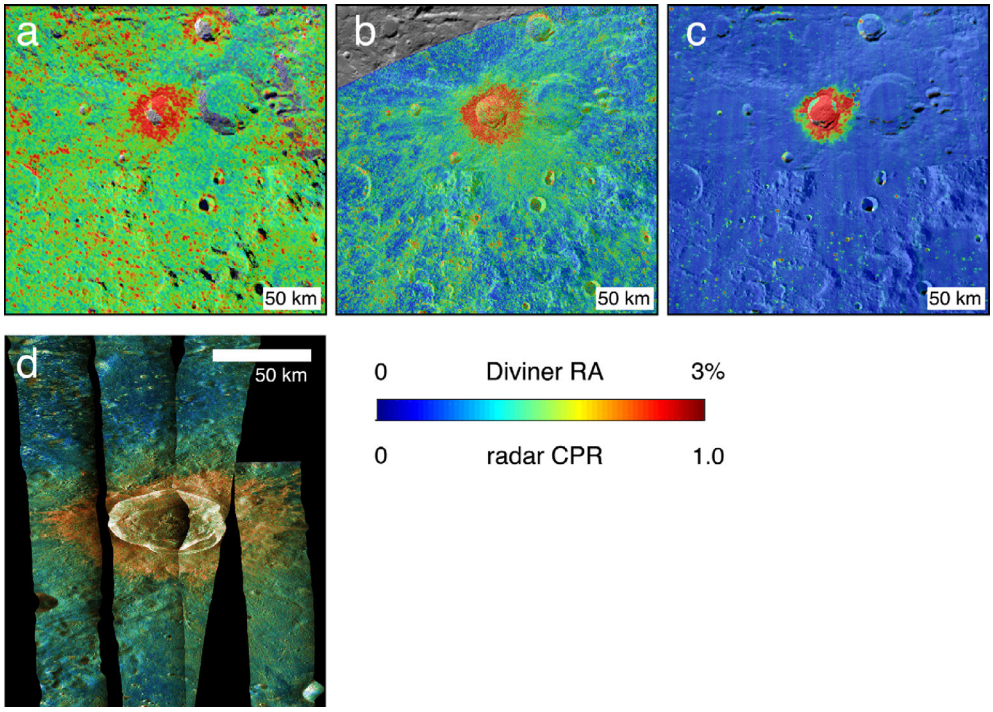

Fig. 6. Crater Thales (50.3 E, 61.7 N, $d = 33.3$ km). (a) AO-GBT P-band CPR, at 400 m/pixel; (b) AO-GBT S-band CPR, at 80 m/pixel; (c) Diviner RA (0–3%); and (d) Mini RF CPR overlain on total power, at 15 m/pixel.

P-band data, indicating that they are too small to be resolved by the longer-wavelength P-band signals. The enhanced signal in S-band CPR data, combined with the low rock abundance values, indicates that the rocks are shallowly buried.

In summary, the near-rim ejecta for our study craters exhibit the full range of measured infrared and radar CPR values, allowing a tens-of-meter scale view of how differently sized rocks are distributed in regolith close to the crater.

4.3. Impact melt

Impact melt commonly occurs as a component of crater ejecta and sometimes forms pools or flows exterior to the crater rim for large craters (e.g., Melosh, 1989). Impact melt has been discussed extensively elsewhere in the literature: previous work has documented the range of possible radar signatures of melt deposits (e.g., Ghent et al., 2008; Campbell et al., 2010; Carter et al., 2012; Neish et al., 2014), and Bandfield et al. (2011) discussed the low rock abundance values associated with the large impact melt sheet at King crater. Here, we consider two end-member age examples, young Giordano Bruno (Fig. 3; age from Morota et al., 2009) and much older Aristoteles (Fig. 7; age from Kirchoff et al., 2013). A melt flow extends 3–4 crater radii northward from the rim of Giordano Bruno and shows high radar backscatter at S-band, along with a lobate morphology that extends 3–4 crater radii beyond the rim. The same feature is apparent in the Diviner rock abundance image, with values of 1–2%; these values are elevated relative to the background terrain but not as high as those found in the continuous ejecta close to the rim (see Section 4.1). This indicates that the melt flow, though rough at cm scales, and despite its youth, is buried beneath a thin layer of regolith, and, as noted by others (e.g., Bandfield et al., 2011; Carter et al., 2012), demonstrates that new regolith forms rapidly on fresh lunar surfaces. Fig. 7 shows a similar melt flow emanating to the north, and a smaller lobe to the NW, from much older Aristoteles. Aristoteles' melt deposits are apparent in both P- and S-band CPR images,

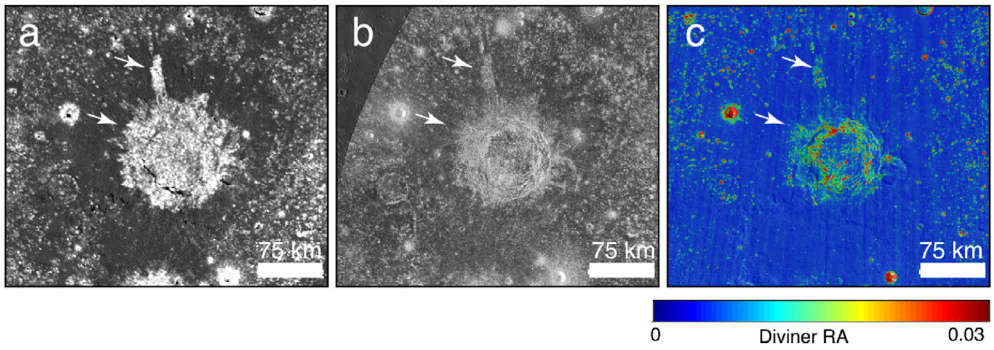

Fig. 7. Crater Aristoteles: AO-GBT P-band CPR (a), AO-GBT S-band CPR (b), and Diviner RA (c) overlain on LROC WAC mosaic. White arrows denote lobate rocky deposits with melt morphology.

indicating the presence of volumetric scatterers or roughness at cm and larger scales. The distal end of the northern flow also shows high rock abundance values, associated with small craters superimposed on the flow. Normally, as discussed in Section 5, the surface ejecta blocks of such old craters have disappeared by ~1 Gyr; but melt flows or pools in the subsurface represent a source of blocks that small craters can excavate. These two examples show how the combination of multi-wavelength radar and Diviner rock abundance data provides a powerful tool for mapping and characterizing otherwise hidden melt deposits of a range of ages.

4.4. Fine ejecta (radar-dark haloes)

4.4.1. Radar versus Diviner rock abundance

Previous work has documented the presence of haloes of low radar return and low radar CPR that appear distal to the radar-bright blocky haloes described above (Thompson et al., 1970, 1974; Schultz and Mendell, 1978; Ghent et al., 2005, 2008, 2010). These features show radar characteristics consistent with depletion in wavelength-scale blocks to the penetration depth of P-band signals, or at least 7 m (Ghent et al., 2005). Fig. 8 shows a number of radar-dark halo craters in the Mare Frigoris region. Their outlines are clearly visible in the P-band radar image (Fig. 8a), extending in general to approximately one crater radius from the parent crater center. Fig. 8b shows a Diviner rock abundance map of the same region. In general, regions away from large craters show low rock abundance values with averages around 0.5%, but regional maps show small regions or individual pixels of slightly elevated values (1–2%), signaling the presence of small craters that excavate meter-scale rocks from underneath or within the regolith. The density of these points is naturally higher in the maria, where relatively thin regolith overlies competent basalt flows, than in the highlands, where thick regolith overlies fragmental megaregolith and fractured bedrock. The radar-dark haloes, however, largely lack these scattered high-rock abundance regions, consistent with earlier interpretations of the haloes as relatively thick deposits of fine-grained, rock-free material.

Previous work has also documented the fact that the margins of radar-dark haloes at P-band are spatially coincident with those found in S-band images (Ghent et al., 2010). This is an important observation that indicates that the halo material must form relatively abrupt terminations, rather than thinning with distance. If halo deposits showed tapering edges, the haloes would appear larger at S-band than at P-band, because the P-band signals require a greater depth of scatterer-free material to produce the observed low return than do S-band signals. Thus, a tapering margin would mean that at some distance from each crater, the deposit would become sufficiently thin to allow P-band signals to reflect from the sub-halo surface while still preventing a basal reflection at S-band. Instead, halo boundaries drawn on P- and S-band images are coincident (Ghent et al., 2010), demonstrating that the radar-dark haloes have sharp distal margins with minimum thicknesses on the order of 7 m (10 P-band wavelengths). We return to this point in Section 6.

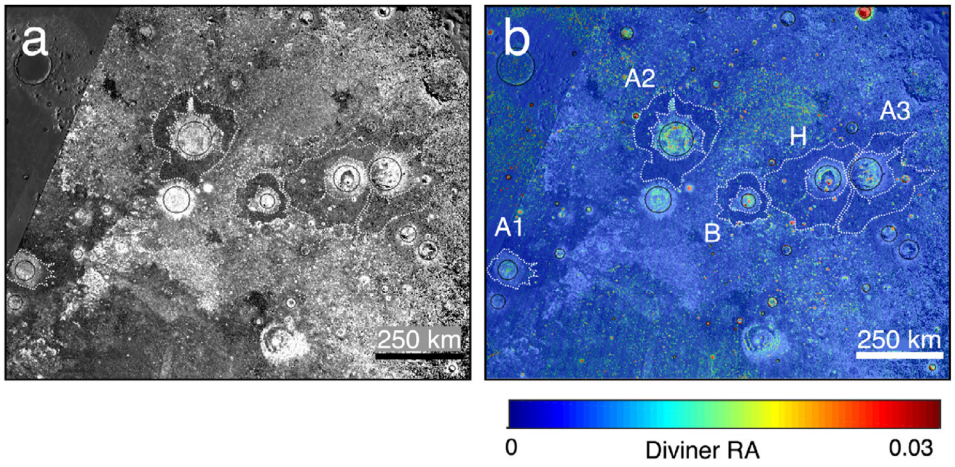

Fig. 8. AO-GBT P-band CPR (a; scaled linearly from 0 to 1) and Diviner RA overlain on LROC WAC (b; scaled 0–3%) images showing radar-dark haloes in the Aristoteles region of Mare Frigoris. Dashed curves outline radar-bright and radar dark ejecta for selected craters: A1: Aristillus, 1.2 E, 33.8 N, $d = 55.9$ km; A2: Aristoteles, 17.2 E, 50.2 N, $d = 94.9$ km; A3: Atlas, 44.4 E, 46.7 N, $d = 93.9$ km; B: Bürg, 28.2 E, 45.0 N, $d = 40.2$ km; H: Hercules, 39.1 E, 46.8 N, $d = 74.0$ km.

4.4.2. Diviner regolith temperature

In addition to Diviner rock abundance maps, the Diviner rock-free regolith temperature data provide information about the shallow structure of the regolith in general, and radar-dark haloes in particular. Like the rock abundance map, the regolith temperature map shows local enhancements corresponding to the presence of small and large craters and steep slopes such as those associated with Vallis Schröteri (Fig. 9). It also shows a pronounced low regolith temperature anomaly centered on a very small crater (white arrow in b); this is an example of a so-called "lunar cold spot" (Bandfield et al., 2014), whose thermophysical characteristics indicate the presence of a surface layer on the order of 2 cm thick with lower density or higher porosity than for typical regolith. Similarly, the pyroclastic deposits that occupy the Aristarchus Plateau (AP) show lower than average regolith temperatures, indicating that in addition to being depleted in surface rocks (a), the plateau has a surface that is even less consolidated in the upper 1–2 cm than typical regolith fines.

The rock abundance map (Fig. 9a) clearly shows a depletion in surface rocks in Aristarchus' radar-dark halo, denoted by the dotted curve, punctuated by isolated rocky spots that correspond to small superimposed craters. The halo regolith temperature, however, is not substantially different from the background terrain. By contrast with the cold spot and the plateau pyroclastic deposits, Aristarchus' radar-dark halo is indistinguishable in regolith temperature from the background terrain. This is true in general for radar-dark haloes, and indicates that the density structure of the upper few cm of halo material is essentially the same as for "typical" regolith (see Hayne et al., 2011; Bandfield et al., 2014).

4.4.3. Small superimposed craters

The low P-band CPR values exhibited by radar-dark haloes indicate that the depletion in wavelength-scale blocks extends to depths of at least ~7 m (10 wavelengths; Ghent et al., 2005, 2010). Furthermore, we know from radar wavelength comparisons that the halo margins are abrupt rather than thinning gradually (Ghent et al., 2010). In principle, we can gain further information about the minimum thickness of radar dark halo material by examining small craters superimposed on the dark haloes. For example, we would expect some small primary craters—those of diameter greater than ~10 times the halo thickness—to excavate blocky subhalo material. Craters that are too small to penetrate the entire halo thickness would not produce any blocks derived from the substrate. As a preliminary assessment of halo thickness, we examine small craters superimposed on radar-dark haloes, looking for variations in the smallest blocky crater with large crater size or distance from the large crater.

Fig. 10a shows an AO-GBT S-band CPR map for Aristarchus, with its bright and dark haloes shown by dotted lines. Small craters that show elevated rock abundance values are also mapped and labeled with their diameters in meters. Though the resolution of the Diviner rock abundance maps is 128 pixels per degree, or ~216 m per pixel at the latitude of Aristarchus crater, the influence on nighttime temperatures of even a few meter-scale or larger rocks covering areas much smaller than one pixel is sufficient to cause a "positive" detection (Bandfield et al., 2011). To confirm this, we examined LROC Narrow Angle Camera (NAC) images for each of the mapped craters, confirming the presence of blocks in each case. An example is shown in frame b, in which two adjacent small craters superimposed on Aristarchus' radar-dark halo appear. The smaller of these two, with diameter 330 m, has no blocks; but the larger, with diameter 430 m, does have blocks. If these craters are small primary craters, and the blocks present in the larger of the two come from the substrate, this case provides a limit on the depth of the halo at that location. If we assume a conservative excavation depth-to-final crater diameter of 1:10 (e.g., Gault et al., 1974), we can conclude that the dark halo at that point is approximately 33 m thick. This is consistent with, but far in excess of, the requirement that haloes be at least 7 m thick to produce the observed signal at 70 cm wavelength. If these craters are secondaries, the excavation depth would be smaller, but still consistent with the minimum 7 m constraint provided by radar observations. If the observed blocks are breccia generated by the impact into particulate material, the implied halo thickness is larger than 1/10 the diameter of the smallest rocky crater, since it would have been the case that this small impact did not penetrate the full halo thickness.

Despite the uncertainties associated with identifying small craters as primary vs. secondary, and the need to constrain the provenance of rocks associated with them, we mapped 325 small rocky craters superimposed on the radar-dark haloes of 15 larger

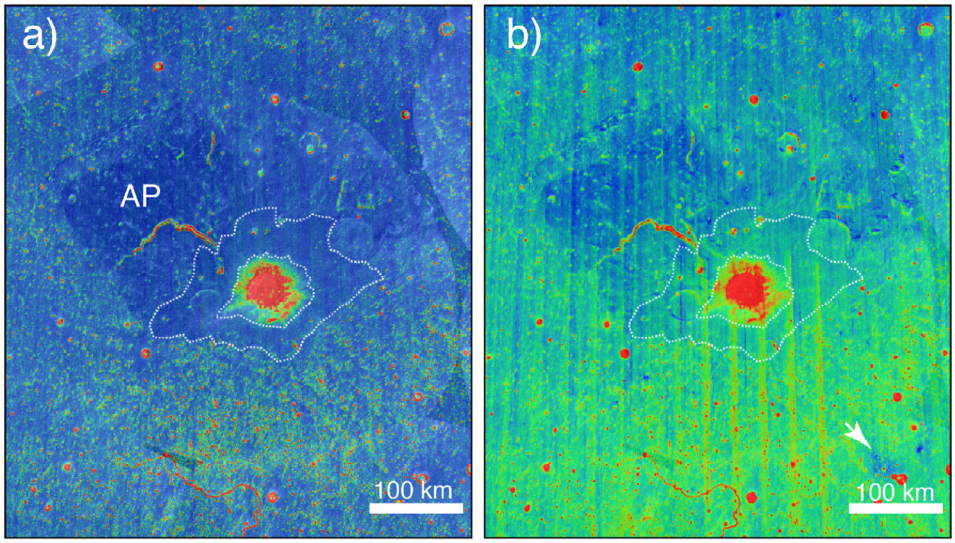

Fig. 9. Diviner RA (a) and rock-free regolith temperature (b) overlain on AO-GBT S-band CPR images. Rock abundance is scaled linearly from 0% (blue) to 3% (red); regolith temperature is linearly scaled from 0 K to 15 K above the latitude- and local time-normalized longitudinal average. Dotted curves denote limits of radar-bright and radar-dark haloes. AP denotes Aristarchus Plateau; the rille Vallis Schröteri appears south of the "AP" label. (For interpretation of the references to color in this figure legend, the reader is referred to the web version of this article.)

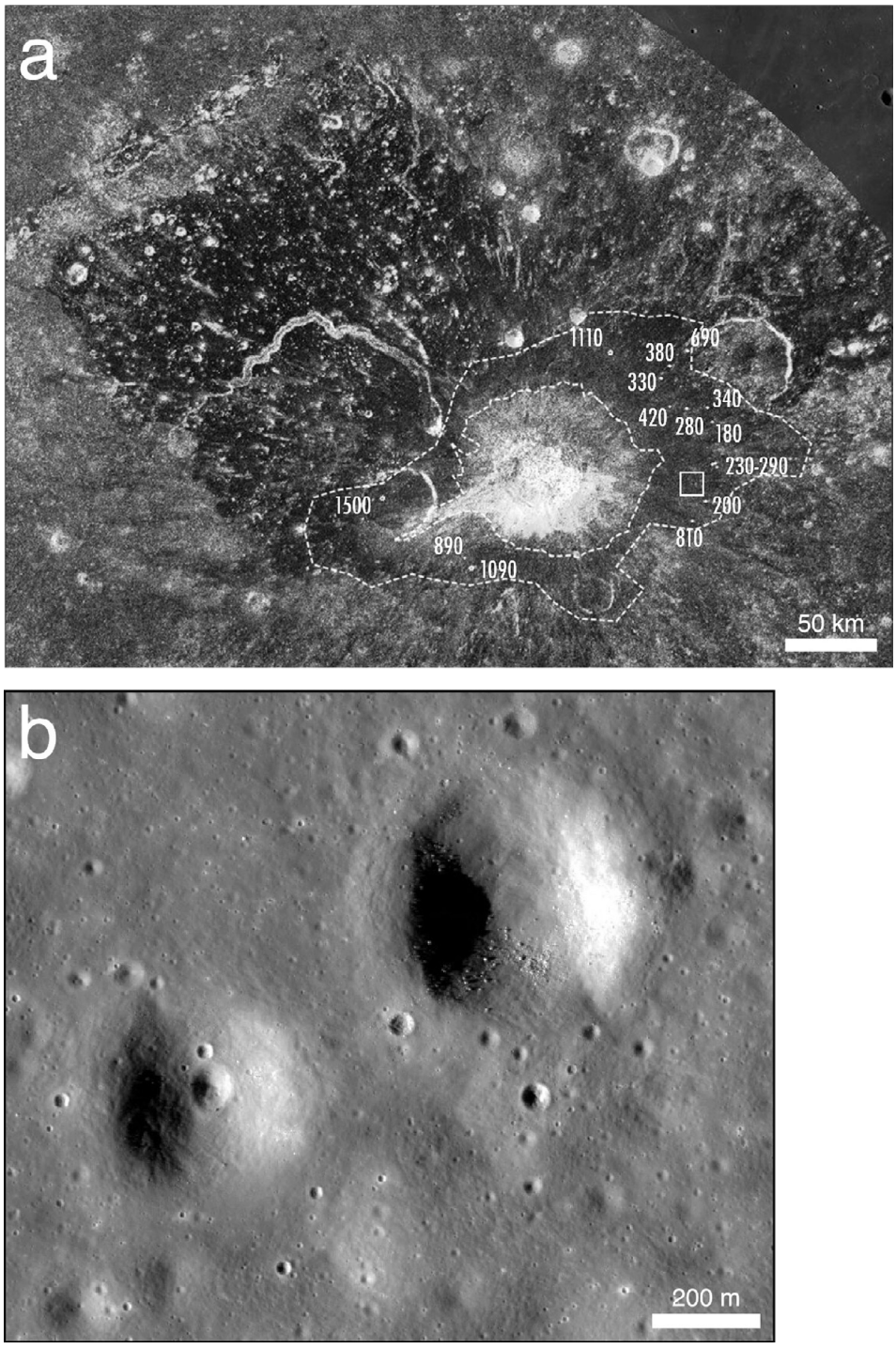

Fig. 10. (a) AO-GBT S-band radar CPR image of Aristarchus crater and plateau, scaled from 0 (black) to 1 (white); dotted outlines indicate limits of bright and dark haloes. Small blocky craters superimposed on the radar-dark halo are shown, with labeled diameters. Box indicates location of (b), which is a portion of LROC NAC image M1112111358LC, and which shows two adjacent small craters with diameters 330 m and 430 m, respectively. The larger of these has excavated blocks that show an elevated Diviner RA signal, whereas the smaller crater shows no blocks.

craters ranging from 8.2 to 94.9 km in diameter. The diameters of superimposed craters that produce blocks range from 160 m to 2000 m. We take the minimum rocky crater diameter for each large crater to represent the minimum halo thickness, understanding that the true halo thickness, whether the small craters are primary or secondary, would lie between the excavation depth of the largest non-rocky crater and that of the smallest rocky crater. We find that the minimum rocky crater size varies from 120 to 320 m, with no clear relationship between that minimum size and parent crater size (Fig. 11). This suggests that all the haloes are, to first order, of similar thickness, independent of the size of the crater with which they are associated. Even if some of the smallest rocky craters identified here are primary and some are secondary, the basic observation of approximate independence of minimum rocky diameter from large crater size holds. A more rigorous treatment of this topic, including analysis

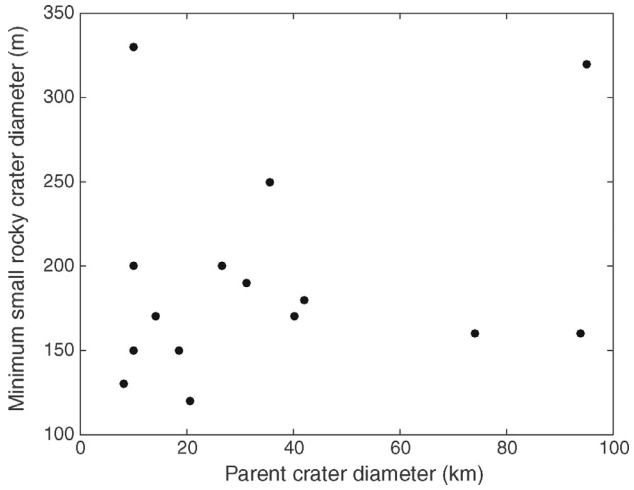

Fig. 11. Plot of minimum diameters of small rocky craters superimposed on larger radar-dark haloes versus halo "parent" crater size (here, "parent" refers to the large crater associated with each radar-dark halo, and does not imply generation of specific secondary craters).

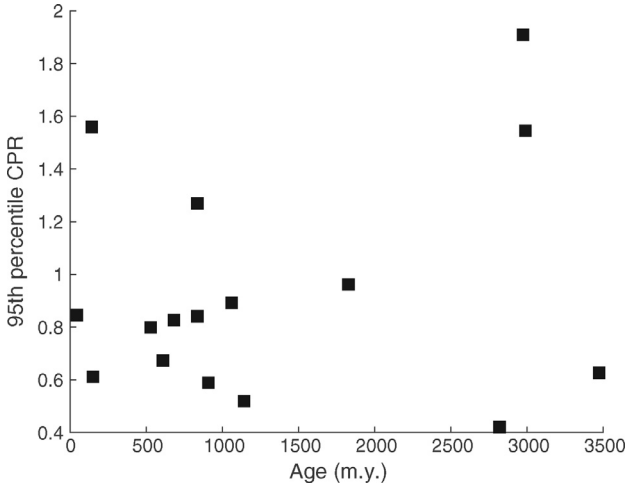

Fig. 12. Plot of 95th percentile P-band CPR value vs. published ages (Baldwin, 1985) for 16 radar-bright ejecta deposits; no correlation between maximum CPR value and age exists.

of small crater morphology, will be carried out in a subsequent contribution.

5. Changes with time

A key question in lunar science is, how fast, and by what processes, does lunar regolith form and overturn? We frame that question in terms of these: how fast do ejecta blocks break down to form fine regolith material, and what is the relative importance of each of the potential breakdown processes, such as micrometeorite bombardment (e.g., Shoemaker et al., 1970; Gault et al., 1972, 1973; Hartung et al., 1972) versus thermal cracking (e.g., Delbo et al., 2014)? What is the fate of ejecta suspended within the regolith? We have previously investigated one aspect of this issue: in Ghent et al. (2014), we established a rate of disappearance of surface rocks, using our observed relationship between ejecta rockiness and crater age for nine large craters with published model ages. In that work, we quantified the rockiness of each crater's ejecta by using the 95th percentile value of the ejecta rock abundance, excluding terrain inward from the crater rim, where steep slopes tend to replenish the surface rock population, and melt ponds, which also provide a source of new rocks via small impacts. We concluded that all surface rocks disappear over a period of roughly 1 byr; for older craters, the ejecta that remain reside in the subsurface, deep enough to be invisible to Diviner.

Here, we investigate this issue for those buried ejecta, using multi-wavelength radar observations. This is challenging, because few individual craters have been dated. Furthermore, published ages are vigorously debated because of inherent uncertainties in the commonly applied method of counting small craters superimposed on crater ejecta or floors, arising from an imperfect knowledge of the crater production function (e.g., Neukum et al., 2001), the effects of variations in target properties (e.g., Williams et al., 2014; van der Bogert, this issue), criteria for distinguishing primary from secondary craters (e.g., Hiesinger et al., 2000; Ivanov, 2006; Bart and Melosh, 2007), and identification of countable units (Hiesinger et al., 2000, 2010, 2012). Furthermore, we lack global radar data coverage. With these caveats in mind, however, we examine radar CPR values as a function of published ages for 16 craters (Fig. 12; Table 1), using the same approach as in Ghent et al. (2014). Even considering that the reported ages are substantially uncertain, no trend like the one we observed for surface rocks from the Diviner rock abundance data is apparent. (It should be noted that the CPR signal we observe, signaling subsurface roughness, could arise either from buried primary ejecta blocks or from blocks generated from a subsurface melt deposit; in either case, there is no variation in the abundance of these blocks with crater age.)

This idea is supported by qualitative evaluation of the radar characteristics of old ejecta deposits. Fig. 13 shows the craters Delisle and Diophantus, with reported ages of 3470 Ma and 659–1208 Ma, respectively (Baldwin, 1985). Both craters, despite having lost their surface rocks, still show haloes of elevated CPR values at both wavelengths. So, too, does Aristoteles (Fig. 7). This indicates that even cm-scale rocks, when buried within the upper meter of regolith, are protected from rock removal processes. The vast majority of the craters visible in Fig. 2 retain their radar-bright P-band haloes. One of the few that clearly shows no remaining blocky ejecta is Vlacq (Fig. 2), dated by counting small craters on its floor at 3.9 ± 0.1 Ga by Kirchoff et al. (2013), who note that the floor terrain on which they counted superimposed craters is most likely not original; hence, this is most likely an underestimate of the true age of the crater. We conclude from these observations that though surface rocks disappear from the Moon on timescales of 1 Gyr, those that are buried within the upper meter to few meters of regolith remain for much longer. This observation is consistent with results of Stickle and Schultz (2012), who predicted that subsurface damage caused by impact is greatly reduced if a thin low-impedance surface layer is present.

Radar-dark haloes also remain in place for much longer than surface rocks. For example, Fig. 14 shows Bullialdus, dated at 2750–3473 Ma by Baldwin (1985). The longevity of radar-dark haloes indicates that steady-state regolith overturn does not act to replenish the haloes' cm- to meter-scale block population, which would render them invisible at radar wavelengths.

6. Discussion

Table 2 summarizes the observations presented here. We draw from these two main conclusions. First, the longevity of both subsurface blocky ejecta and radar-dark halo material places an important constraint on the process of regolith overturn. In the canonical view (e.g., Gault et al., 1973, 1974), the lunar surface is bombarded by small bolides at a rate governed by the incoming

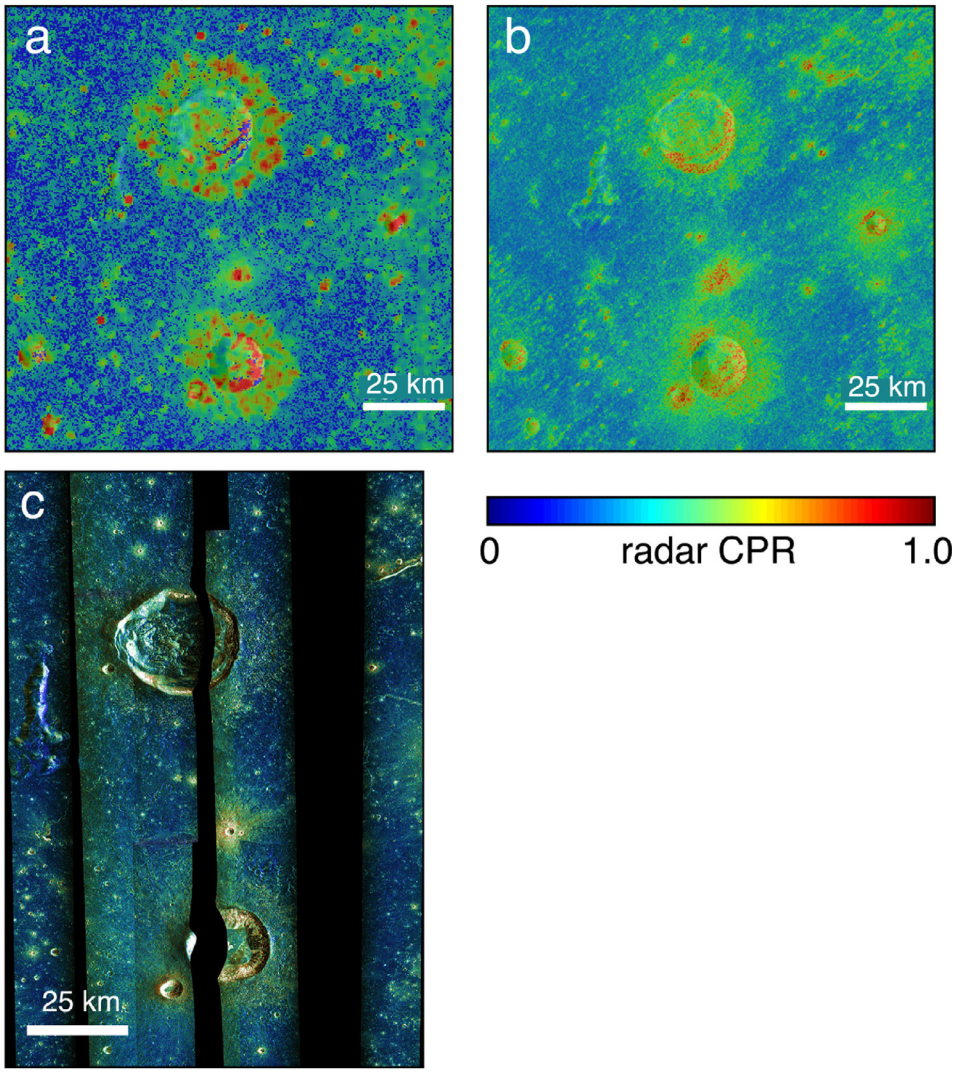

Fig. 13. (a) AO-GBT P-band; (b) AO-GBT S-band; and (c) Mini RF S-band CPR images of craters Delisle (top) and Diophantus (bottom). Both craters' ejecta still show high CPR signatures associated with blocky subsurface ejecta despite having lost their surface rocks. Model ages: Delisle, 3470 Ma; Diophantus, 659–1208 Ma (Baldwin, 1985).

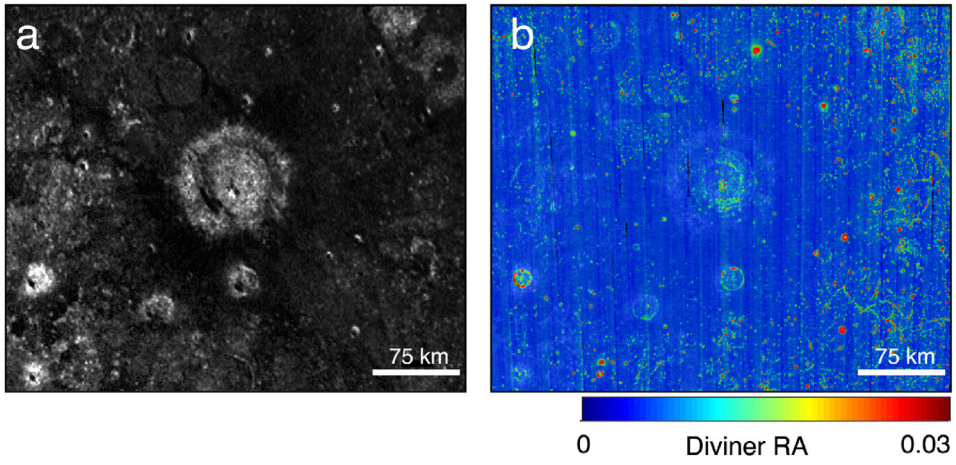

Fig. 14. (a) AO-GBT P-band CPR and (b) and Diviner RA images of crater Bullialdus (337.7 E, −20.8 N, $d = 62.5$ km) showing pronounced radar-dark (a) and surface rock-free (b) halo. Age: 2750–3473 Ma (Baldwin, 1985).

size-dependent flux of material. Gault et al. (1974) used this size dependence to calculate rates of overturn at various depths, with the top mm of regolith being predicted to be overturned once every 10^4 years, and the top 10 cm overturned once in 1 Gyr. According to these models, it takes on the order of 4 Gyr to turn the regolith over to a depth of 20 m, the approximate depth of

Table 2
Summary of ejecta properties.

Proximal blocky ejecta	Fine distal ejecta
High radar backscatter and CPR	Low radar backscatter and CPR
Surface rocks apparent for young craters; disappear over 1 Gyr timescale	Depleted in surface rocks for both young and old craters
Subsurface rocks apparent for older craters; remain intact for much longer	
Margins appear in different places at different wavelengths, reflecting local variations in block size and burial depth	Locations of margins are independent of wavelength, indicating abrupt margins
	Depth as reflected by small superimposed rocky craters approximately independent of parent crater size

the radar-dark haloes, one time. Our results support these general rates; the survival of both subsurface blocky ejecta (composed of at least cm-scale rocks in order to appear radar-bright at S-band) and radar-dark haloes to ages approaching 4 Gyr implies that impact events large enough to disrupt the large spatial areas they occupy are rare. By contrast, the rates calculated by Gault et al. (1974) predict that at 5 cm depth, the regolith is overturned 100 times in 1 Gyr, and 10^4 times in 1 Gyr at 1 mm depth, consistent with removal of surface rocks over this timescale, as observed (Ghent et al., 2014). Small rocks buried to depths of even tens of cm are predicted to survive for long periods, as we find here. Improved age constraints for individual craters, which are certain to result from the availability and extensive coverage of high resolution LRO Camera images and other new datasets, could help us more robustly quantify the survival times of buried rocks.

Second, the observation that the minimum thickness of radar-dark halo material, is, to first order, independent of crater size, leads to a new understanding of its mechanism of emplacement. This observation, together with the aforementioned sharpness of the halo outer margins, precludes the tempting notion that the halo is comprised of ballistically emplaced material from within the crater cavity, as has previously been proposed (Ghent et al., 2010), because that mechanism would produce a deposit that thinned with distance from the source, producing a feathered margin (e.g., McGetchin et al., 1973; Melosh, 1989), and whose minimum thickness should vary with crater size. Instead, the minimum thickness must be governed by some physical factor that is independent of crater size. The radar-dark haloes' abrupt boundaries suggest an energy- or momentum-limited flow process, such as a ground-hugging granular flow. Oberbeck (1975), in his discussion of "ballistic sedimentation," points out that material in the primary ejecta curtain interacts with and incorporates local material as it sweeps outward from the impact site. We propose that fragmental ejecta hitting the surface mobilize existing regolith, and it is this process, together with collisional grinding within the ejecta curtain and during the interaction with the surface, that produces the observed halo material (cf. Schultz and Mendell, 1978). The resulting halo material is depleted in decimeter-scale and larger rocks, and blankets the pre-existing terrain to depths on the order of 10–30 m. It forms a ground-hugging flow that travels en masse to a runout distance governed by its momentum, which is ultimately determined by the mass and velocity of ejecta particles hitting the pre-existing surface. The halo material is therefore composed of a mixture of ejecta and pre-existing regolith, which is largely rock-free to begin with; any remaining rocks are either ground down within the flow, or buried by it. The fraction of material originating from within the crater cavity relative to pre-existing regolith is difficult to determine. Assuming that the haloes take the form of disks with uniform thickness, their volumes are 1–2 orders of magnitude smaller than calculated total transient cavity volumes. Depending on the fraction of that transient crater volume represented by ejected material, the dark haloes may represent a significant fraction of the total mass ejected.

Schultz and Mendell (1978) also point out that ejecta from large craters at a given distance (relative to crater size) experience higher peak shock pressures than ejecta from smaller craters. This should lead to smaller average particle sizes at a given relative range for larger craters. We propose that the impact of these smaller ejecta would have a smaller effect on the pre-existing regolith than would larger particles; and therefore, we would expect smaller radar-dark haloes, relative to crater size, for larger craters. Indeed, Ghent et al. (2010) showed that the maximum dark halo size scales as $R^{-0.18}$, where R is crater radius. The observations presented here, together with previous work by Schultz and Mendell (1978) and others, provide a basis for modeling this process, which would yield significant new insight into the behavior of ejecta and their effects on the surrounding terrain.

References

Baldwin, R.B., 1985. Relative and absolute ages of individual craters and the rate of infalls on the Moon in the post-imbrium period. Icarus 61, 63–91. doi:10.1016/0019-1035(85)90156-3, (ISSN 0019-1035).

Bandfield, J.L., et al., 2011. Lunar surface rock abundance and regolith fines temperatures derived from LRO Diviner Radiometer data. J. Geophys. Res. 116, E00H02. doi:10.1029/2011JE003866.

Bandfield, J.L., et al., 2014. Lunar cold spots: Granular flow features and extensive insulating materials surrounding young craters. Icarus 231, 221–231. doi:10.1016/j.icarus.2013.12.017.

Baratoux, D., et al., 2005. Thermal properties of lobate ejecta in Syrtis Major, Mars: Implications for the mechanisms of formation. J. Geophys. Res.: Planets 110. doi:10.1029/2004JE002314.

Barlow, N.G., 2006. Impact craters in the northern hemisphere of Mars: Layered ejecta and central pit characteristics. Meteorit. Planet. Sci. 41, 1425–1436. doi:10.1111/j.1945-5100.2006.tb00427.x.

Bart, G.D., Melosh, H.J., 2007. Using lunar boulders to distinguish primary from distant secondary impact craters. Geophys. Res. Lett. 34, L07203. doi:10.1029/2007GL029306.

Cahill, J.T.S., et al., 2014. The Miniature Radio Frequency instrument's (Mini-RF) global observations of Earth's moon. Icarus 243, 173–190. doi:10.1016/j.icarus.2014.07.018.

Campbell, B.A., 2002. Radar Remote Sensing of Planetary Surfaces. Cambridge University Press.

Campbell, B.A., 2012. High circular polarization ratios in radar scattering from geologic targets. J. Geophys. Res. 117, E06008. doi:10.1029/2012JE004061.

Campbell, B.A., et al., 2007. Focused 70-cm wavelength radar mapping of the Moon. IEEE Trans. Geosci. Remote Sens. 45, 4032–4042. doi:10.1109/TGRS.2007.906582.

Campbell, B.A., et al., 2010. Earth-based 12.6-cm wavelength radar mapping of the Moon: New views of impact melt distribution and mare physical properties. Icarus 208, 565–573. doi:10.1016/j.icarus.2010.03.011.

Carter, L.M., et al., 2012. Initial observations of lunar impact melts and ejecta flows with the Mini-RF radar. J. Geophys. Res.: Planets 117. doi:10.1029/2011JE003911.

Delbo, M., et al., 2014. Thermal fatigue as the origin of regolith on small asteroids. Nature 508, 233–236. doi:10.1038/nature13153.

Gault, D.E., Hörz, F., Hartung, J.B., 1972. Effects of microcratering on the lunar surface, Proc. Lunar Sci. Conf. 3, 2713–2734 (Suppl. 3, Geochim. Cosmochim. Acta).

Gault, D.E., Hörz, F., Hartung, J.B., 1973. Abrasion and catastrophic rupture of lunar rocks: Some implications to the micrometeoroid flux at 1 AU. In: Space Research Conference – 1, pp. 1085–1093.

Gault, D.E. et al., 1974. Proc. Lunar Sci. Conf. 3, 2365–2386 (Suppl. 5, Geochim. Cosmochim. Acta).

Ghent, R.R., et al., 2005. Earth-based observations of radar-dark crater haloes on the Moon: Implications for regolith properties. J. Geophys. Res. 110, E02005. doi:10.1029/2004JE002366.

Ghent, R.R., et al., 2008. Earth-based radar data reveal extended deposits of the Moon's Orientale basin. Geology 36, 343. doi:10.1130/G24325A.1.

Ghent, R.R., et al., 2010. Generation and emplacement of fine-grained ejecta in planetary impacts. Icarus 209, 818–835. doi:10.1016/j.icarus.2010.05.005.

Ghent, R.R., et al., 2014. Constraints on the recent rate of lunar ejecta breakdown and implications for crater ages. Geology 42, 1059–1062. doi:10.1130/G35926.1.

Hartung, J.B., Hörz, F., Gault, D.E., 1972. Lunar microcraters and interplanetary dust. Proc. Lunar Sci. Conf. 3, 2735.
Hawke, B.R., Bell, J.F., 1982. Remote sensing studies of lunar dark-halo impact craters – Preliminary results and implications for early volcanism. Lunar Planet. Sci. 12, 665–678.
Hayne, P.O. et al., 2011. The Moon's extremely insulating near-surface: Diviner infrared observations of a total lunar eclipse. American Geophysical Union (Fall). Abstract 1712.
Hiesinger, H., et al., 2000. Ages of mare basalts on the lunar nearside. J. Geophys. Res. 105, 29239–29276. doi:10.1029/2000JE001244.
Hiesinger, H., et al., 2010. Ages and stratigraphy of lunar mare basalts in Mare Frigoris and other nearside maria based on crater size–frequency distribution measurements. J. Geophys. Res. 115, E03003. doi:10.1029/2009JE003380.
Hiesinger, H., et al., 2012. How old are young lunar craters? J. Geophys. Res. 117, E00H10. doi:10.1029/2011JE003935.
Ivanov, B.A., 2006. Earth/Moon impact rate comparison: Searching constraints for lunar secondary/primary cratering proportion. Icarus 183, 504–507. doi:10.1016/j.icarus.2006.04.004.
Kirchoff, M.R., et al., 2013. Ages of large lunar impact craters and implications for bombardment during the Moon's middle age. Icarus doi:10.1016/j.icarus.2013.03.018.
McGetchin, T.R., Settle, M., Head, J.W., 1973. Radial thickness variation in impact crater ejecta: Implications for lunar basin deposits. Earth Planet. Sci. Lett. 20, 226–236. doi:10.1016/0012-821X(73)90162-3.
Melosh, H.J., 1989. Impact cratering: A geologic process. Oxford Monographs on Geology and Geophysics, vol. 11. Oxford University Press, New York.
Morota, T., et al., 2009. Formation age of the lunar crater Giordano Bruno. Meteorit. Planet. Sci. 44, 1115–1120. doi:10.1111/j.1945-5100.2009.tb01211.x.
Neish, C.D., et al., 2014. Global distribution of lunar impact melt flows. Icarus 239, 105–117. doi:10.1016/j.icarus.2014.05.049.
Neukum, G., Ivanov, B.A., Hartmann, W.K., 2001. Cratering records in the inner Solar System in relation to the lunar reference system. Space Sci. Rev. 96, 55–86.
Nowicki, S.A., Christensen, P.R., 2007. Rock abundance on Mars from the Thermal Emission Spectrometer. J. Geophys. Res. 112, E05007. doi:10.1029/2006JE002798.
Oberbeck, V.R., 1975. The role of ballistic erosion and sedimentation in lunar stratigraphy. Rev. Geophys. 13 (2), 337–448.
Paige, D.A., et al., 2009. The Lunar Reconnaissance Orbiter Diviner lunar radiometer experiment. Space Sci. Rev. 150, 125–160. doi:10.1007/s11214-009-9529-2.
Quaide, W.L., Oberbeck, V.R., 1968. Thickness determinations of the lunar surface layer from lunar impact craters. J. Geophys. Res. 73, 5247. doi:10.1029/JB073i016p05247.
Raney, R.K., et al., 2011. The lunar Mini-RF radars: Hybrid polarimetric architecture and initial results. Proc. IEEE 99, 808–823. doi:10.1109/JPROC.2010.2084970.
Schultz, P.H., Mendell, W., 1978. Orbital infrared observations of lunar craters and possible implications for impact ejecta emplacement. Lunar Planet. Sci. 9, 2857–2883.
Shoemaker, E.M., et al., 1970. Origin of the lunar regolith at Tranquillity Base. Geochim. Cosmochim. Acta Suppl. 1, 2399–2412.
Shorthill, R.W., Thompson, T.W., Zisk, S.H., 1972. Infrared and radar maps of the lunar equatorial region. Moon 4, 442–446. doi:10.1007/BF00562010.
Stickle, A.M., Schultz, P.H., 2012. Subsurface damage from oblique impacts into low-impedance layers doi:10.1029/2011JE004043, E07006.
Stöffler, D., Ryder, G., 2001. Stratigraphy and isotope ages of lunar geologic units: Chronological standard for the inner Solar System. In: Chronology and Evolution of Mars, Space Sciences Series of ISSI. Springer, Netherlands, Dordrecht, pp. 9–54. doi:10.1007/978-94-017-1035-0_2.
Thompson, T.W., et al., 1970. Radar maps of the Moon at 70-cm wavelength and their interpretation. Radio Sci. 5, 253–262. doi:10.1029/RS005i002p00253.
Thompson, T.W., et al., 1974. A comparison of infrared, radar, and geologic mapping of lunar craters. Moon 10, 87–117 (Springer).
Thompson, T.W., et al., 1979. Blocky craters – Implications about the lunar megaregolith. Moon Planets 21, 319–342. doi:10.1007/BF00897360.
Thompson, T.W., et al., 1981. Lunar craters with radar bright ejecta. Icarus 46, 201–225.
van der Bogert, C. H., Hiesinger H., Dundas C., Krüger T., McEwen A. S., Zanetti M., Robinson M. S. Origin of discrepancies between crater size-frequency distributions of Coeval Lunar Geologic Units via Target Property Contrasts Manuscript. Icarus-14423.
van der Bogert, C.H. et al., 2010. Discrepancies between crater size–frequency distributions on ejecta and impact melt pools at lunar craters: An effect of differing target properties? Lunar Planet. Sci. 41, 2165.
van der Bogert, C.H. et al., 2013. New evidence for target property influence on crater size–frequency Distribution measurements. Lunar Planet. Sci. 44, 1962.
Wada, K., Barnouin-Jha, O.S., 2005. The formation of fluidized ejecta on Mars by granular flows. Meteorit. Planet. Sci. 41, 1551–1569.
Wilhelms, D.E., 1987. The Geologic History of the Moon. Volume 1348 of Professional Paper/Department of the Interior, United States Geological Survey, U.S. Government Printing Office, 302 pp.
Williams, J.-P., Pathare, A.V., Aharonson, O., 2014. The production of small primary craters on Mars and the Moon. Icarus 235, 23–36. doi:10.1016/j.icarus.2014.03.011.